PHOTONICS Research

Room temperature optical mass sensor with an artificial molecular structure based on surface plasmon optomechanics

Jian Liu[1,2,3] and Ka-Di Zhu[1,2,3,*]

[1]Key Laboratory of Artificial Structures and Quantum Control (Ministry of Education), Shanghai 200240, China
[2]School of Physics and Astronomy, Shanghai Jiao Tong University, Shanghai 200240, China
[3]Collaborative Innovation Center of Advanced Microstructures, Nanjing 210000, China
*Corresponding author: zhukadi@sjtu.edu.cn

Received 17 April 2018; revised 28 May 2018; accepted 5 June 2018; posted 7 June 2018 (Doc. ID 328537); published 9 August 2018

We propose an optical weighing technique with a sensitivity down to a single atom through the coupling between a surface plasmon and a suspended graphene nanoribbon resonator. The mass is determined via the vibrational frequency shift on the probe absorption spectrum while the atom attaches to the nanoribbon surface. We provide methods to separate out the signals of the ultralow frequency vibrational modes from the strong Rayleigh background, first based on the quantum coupling with a pump-probe scheme. Owing to the spectral enhancement in the surface plasmon and the ultralight mass of the nanoribbon, this scheme results in a narrow linewidth (∼GHz) and ultrahigh mass sensitivity (∼30 yg). Benefitting from the low noises, our optical mass sensor can be achieved at room temperature and reach ultrahigh time resolution.

OCIS codes: (120.4880) Optomechanics; (240.6680) Surface plasmons; (350.4238) Nanophotonics and photonic crystals; (300.6210) Spectroscopy, atomic.

https://doi.org/10.1364/PRJ.6.000867

1. INTRODUCTION

Since its development over 30 years ago, surface-enhanced Raman scattering (SERS) has attracted much attention due to its high sensitivity in detecting the structure of materials [1–5]. Compared to normal Raman scattering, SERS can enhance normally weak Raman signals by several orders of magnitude and has evolved into a powerful and reliable analytical tool for the ultrasensitive detection of analytes, even at the single-molecule level [6–9]. Numerous experimental and theoretical works have focused on the enhancement mechanism. Recently, Roelli *et al.* introduced the cavity optomechanics model that accounts for the dynamical nature of the plasmon-molecule interaction. This will lead to a nonlinear enhancement of Raman emission that is not predicted by conventional theory [10]. It allows the design of novel molecular quantum optomechanical systems and unconventional optical nanodevices.

On the other hand, nanoelectromechanical systems have been proposed for highly sensitive mass detection of neutral species. Significant progress has been made in using nanofabricated resonators [11,12] and carbon nanotubes [13–15]. Graphene has properties that are extremely sensitive to the environment. Thus, it is natural to consider using graphene for sensor applications for probing quantum limit motion [16], mass [13–15], and force [17]. So far, the best mass resolution achieved experimentally with microfabricated resonators has been 200 yg at room temperature [14], whereas carbon nanotube resonators have achieved mass resolution as low as 2 yg in base pressure of 3×10^{-11} mbar at a temperature of about 50 K [15].

Here we demonstrate an all-optical method to determine the inertial mass of atomic species (∼30 yg) via a doubly clamped armchair-edge suspended graphene nanoribbon resonator (SGR) coupled to the plasmon. This device can be achieved at room temperature, and the probe signal can be enhanced remarkably via the plasmonic coupling. Theoretical analysis predicts that a sensitivity comparable to the mass of one Ne atom should be feasible, which would open up the possibility of distinguishing between different chemical elements in future inertial mass spectrometry.

In the previous mass sensing procedures using two-level systems, the exciton is considered as a two-level system in the carbon nanotube, and it couples to the phonons in the nanotube. One can obtain the signal absorption peak of the exciton under the pump field in the coupling system of the exciton and phonons [18]. The enhancement is based on the optical dynamics of excitons in a system of strongly coupled excitons and plasmons [19]. The mass detection using plasmonic cavity in this paper is totally different. Here we map the SERS scenarios onto the canonical model of cavity optomechanics, in which a

dynamic interaction takes place between two parametrically coupled and nonresonant harmonic oscillators, namely, the molecular vibration and the localized plasmons. Thus, we consider the plasmon mode as a cavity mode. The signal enhancement is based on the strong coupling between the plasmon cavity and the suspended graphene nanoribbon (i.e., artificial molecular vibration). This system is simpler and more convenient than the previous work, since there is no need for the exciton. Moreover, the coupling between the exciton and nanoresonator is usually very weak (~MHz) [18], while one can obtain strong optomechanical coupling (~10^2 GHz) and thus strong enhancement with the plasmonic nanocavity.

Compared with traditional electrical mass detection [11–15], there are many incomparable advantages for this optical mass sensing. For example, the heat effect and energy loss caused by circuits can be removed during the optical mass measurement, the spectral width in optical sensing (~0.5 GHz) is narrower than in electrical technique, and the ultrashort measuring time (~2 ns) allows ultrahigh time resolution. Furthermore, other than the single optical mass detection, the all-optical mass sensing is not restricted by the vibrational frequency of nanomechanical resonator, which will break many limitations of the electrical method and single optical measurement. The all-optical mass sensing provides a new platform in nanoscale measurement and promises to enhance mass sensitivity and accuracy in the future.

2. THEORETICAL FRAMEWORK

Following the theoretical framework introduced in Ref. [10], we consider the parametric coupling between the plasmon and the vibration of the SGR in the molecular optomechanical system with the simultaneous presence of a strong pump field and a weak probe pulse; the typical physical situation is shown in Fig. 1(a). The armchair graphene nanoribbon is clamped on two edges. This SGR can vibrate in the gigahertz

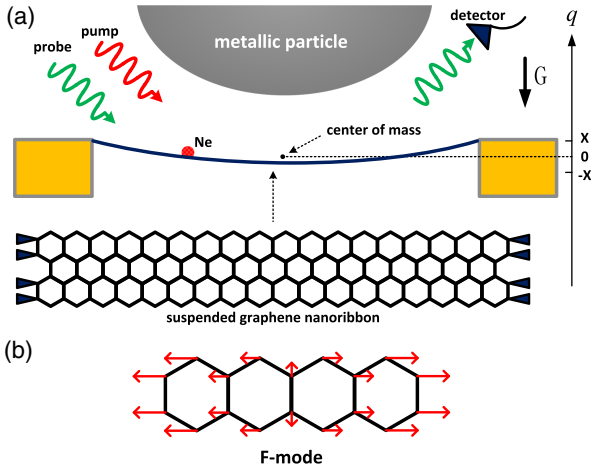

Fig. 1. (a) Schematic diagram of the suspended graphene nanoribbon placed in the surface plasmonic cavity with presence of a strong pump beam and a weak probe beam; G points the direction of the gravity. The Ne atoms are deposited onto the surface of the graphene sheet in a special evaporator. (b) Displacement pattern of the atoms in the graphene nanoribbon due to the fundamental in-plane flexural resonance mode.

band (about 0.03–100 cm^{-1}), corresponding to the fundamental in-plane flexural resonance [20,21]. We define this ultralow frequency (ULF) vibration mode in SGR as the flexural mode (F-mode).

The lowest energy level of the F-mode of SGR can be well described by a harmonic oscillator with fundamental frequency ω_m. The corresponding Hamiltonian is $H_m = \hbar\omega_m a^+ a$, where a^+ and a are the bosonic creation and annihilation operators, respectively. The Hamiltonian of the localized plasmon mode with resonance frequency ω_c can be expressed as $H_c = \hbar\omega_c c^+ c$ with c^+ and c as bosonic creation and annihilation operators. The coupling of the SGR and the plasmonic mode is parametric. The Hamiltonian of interaction term can be written as $H_{\text{int}} = -\hbar\Psi \cdot x_{\text{ZPF}} c^+ c(a^+ + a)$, where Ψ is the optomechanical coupling rate, and $x_{\text{ZPF}} = \sqrt{\hbar/2m\omega_m}$ is the zero-point motion. We assume that the SGR is located at the position of maximum electric field, to leading order; Ψ is given by $\Psi = -\frac{\omega_c}{\epsilon_0 V_c}\frac{\partial\alpha}{\partial x}$, where the polarizability α is a material property that depends on the molecular structure and nature of the bonds, and V_c is the mode volume of the plasmon cavity. If we use the mass-weighted Cartesian displacement coordinates $q = \sqrt{m}x$, the coupling can be quantified by the optomechanical vacuum coupling rate in SI units [10]

$$g = \Psi \cdot x_{\text{ZPF}} = \frac{\partial\alpha}{\partial q}\frac{\omega_c}{\epsilon_0 V_c}\sqrt{\frac{\hbar}{2\omega_m}}. \tag{1}$$

In order to compute g, we need to consider the Raman activity $R = (\partial\alpha/\partial q)^2$, which is a pure molecular property and independent of the experimental setup. In simulations, using Gaussian units, this quantity is expressed as $Å^4 \cdot amu^{-1}$. The relation between the two is given by $R[\text{SI}] = (4\pi\epsilon_0)^2(10^{-13}/1.66)R(\text{g.u.})$.

In a simple classical description, the magnitude of the Raman response of a vibrational mode is proportional to the rate of change of polarizability α in the normal coordinate q, evaluated at the equilibrium position ($q = 0$) of the "mass of center", as shown in Fig. 1(a). In the following discussion, we define q as the direction parallel to the gravity. During the mechanical vibrational motions, the atomic positions in the SGR are schematically changed. This results in a breathing-like expansion and compression of the graphene sheet, as shown in Fig. 1(b). For the F-mode, the SGR structure exhibits distinct atomic configurations and hence, different polarizability at $q = x$ and $q = -x$; here, $x = \sqrt{k_B T/(m\omega_m^2)}$ is the root mean square amplitude of the vibrational graphene sheet at thermal equilibrium. It leads to a nonzero derivative of polarizability and hence a finite Raman response. The symmetry of this breathing-like mode is A_g[22].

The Hamiltonian of the plasmon coupled with two optical fields can be given as $H_{\text{opt}} = -i\hbar\Omega_p(c - c^+) - i\hbar\Omega_s(ce^{i\delta t} - c^+ e^{-i\delta t})$, where Ω_p and Ω_s are coherent driving parameters of the pump field and probe field, respectively, which can be calculated by [23]

$$\Omega_j = \frac{1}{4\pi}\sqrt{\frac{3\epsilon_0\lambda^3}{2\hbar}\eta\kappa}|E_j|, \qquad j = p, s. \tag{2}$$

Here, ϵ_0 is the vacuum permittivity, $\eta \approx 0.01$ is the conservative quantum yield of a dipolar emitter placed in such

cavity, κ is the damping rate of the plasmon cavity, and E_p (E_s) is the amplitude of the pump (probe) illumination. The probe is much weaker than the pump in the experiments; thus, we choose $E_s \sim 10^{-2}E_p$.

Based on the analysis above, the Hamiltonian of the whole system can be expressed as

$$H = H_c + H_m + H_{\text{int}} + H_{\text{opt}}. \tag{3}$$

In a frame rotating at the pump field frequency ω_c, the Hamiltonian can be written as

$$\begin{aligned} H = {} & \hbar\Delta_p c^+ c + \hbar\omega_m a^+ a - \hbar g c^+ c(a^+ + a) \\ & - i\hbar\Omega_p(c - c^+) - i\hbar\Omega_s(ce^{i\delta t} - c^+ e^{-i\delta t}), \end{aligned} \tag{4}$$

where $\Delta_p = \omega_p - \omega_c$ is pump-cavity detuning and the detuning of the probe and pump field can be defined as $\delta = \omega_s - \omega_p$. In what follows, we define the operator $n = a^+ + a$ and deal with the mean response of the system in the presence of the coupling. Let $\langle c\rangle$, $\langle c^+\rangle$, and $\langle n\rangle$ be the expectation values of operators c, c^+, and n, respectively. According to the Heisenberg equation of motion and the communication relations $[c, c^+] = 1$, $[a, a^+] = 1$, the temporal evolutions of a and n can be obtained by solving the quantum Langevin equations with the damping terms

$$\frac{\mathrm{d}c}{\mathrm{d}t} = -(i\Delta_p + \kappa)c + ignc + \Omega_p + \Omega_s e^{-i\delta t} + \sqrt{\kappa}\hat{a}_{in}, \tag{5}$$

$$\frac{\mathrm{d}^2 n}{\mathrm{d}t^2} + \gamma\frac{\mathrm{d}n}{\mathrm{d}t} + \omega_m^2 n = 2\omega_m g c^+ c + \hat{\xi}(t), \tag{6}$$

where γ is the damping rate of the vibrational mode of the SGR. In Eq. (5), a_{in} is the δ-correlated Langevin noise operator of the cavity-field quantum vacuum fluctuation, which has zero mean

$$\langle \hat{a}_{in}(t)\hat{a}_{in}^+(t')\rangle = \delta(t - t'), \tag{7}$$

$$\langle \hat{a}_{in}^+(t)\hat{a}_{in}(t')\rangle = 0. \tag{8}$$

The motion of SGR is affected by a thermal bath of Brownian and non-Markovian stochastic processes. The quantum effects on the resonator are only displayed in the limit of very high quality factor. The resonator mode is affected by a Brownian stochastic force with zero mean value, and $\hat{\xi}(t)$ has the correlation function [24]

$$\langle \hat{\xi}^+(t)\hat{\xi}(t')\rangle = \int \frac{\kappa\omega \mathrm{d}\omega}{\omega_m 2\pi} e^{-i\omega(t-t')}\left[1 + \coth\left(\frac{\hbar\omega}{2k_B T}\right)\right]. \tag{9}$$

Here k_B is Boltzmann's constant, and T is the effective resonator temperature. Following standard methods from quantum optics, we derive the steady-state solutions to Eqs. (5) and (6) by setting all the time derivatives to zero

$$c_0 = \frac{\Omega_p}{(i\Delta_p + \kappa) - ign}, \qquad n_0 = \frac{2g|c|^2}{\omega_m}. \tag{10}$$

We define the parameter $\omega_0 = |c_0|^2$; hence, we can obtain

$$\Omega_p^2 = \omega_0\left[\kappa^2 + \left(\Delta_p - \frac{g^2\omega_0}{\omega_m}\right)^2\right]. \tag{11}$$

One can always rewrite each Heisenberg operator as the sum of its steady-state mean value and a small fluctuation with zero mean value as follows:

$$c = c_0 + \delta c, \qquad n = n_0 + \delta n. \tag{12}$$

Inserting these equations into the Langevin equations, one can safely neglect the nonlinear terms such as $\delta c\delta n$. Since the driving fields are weak, we will identify all operators with their expectation values and drop the quantum and thermal noise terms. Then the linearized Langevin equations can be written as

$$\langle \delta\dot{c}\rangle = -\kappa\langle\delta c\rangle + ig(n_0\langle\delta c\rangle + c_0\langle\delta n\rangle) + \Omega_p + \Omega_s e^{-i\delta t}, \tag{13}$$

$$\langle \delta\ddot{n}\rangle + \gamma\langle\delta\dot{n}\rangle + \omega_m^2\langle\delta n\rangle = 2\omega_m g c_0^2. \tag{14}$$

To solve these equations, we make the ansatz as follows:

$$\langle\delta c\rangle = c_+ e^{-i\delta t} + c_- e^{i\delta t}, \tag{15}$$

$$\langle\delta n\rangle = n_+ e^{-i\delta t} + n_- e^{i\delta t}. \tag{16}$$

Upon substituting these equations into Eqs. (13) and (14), and upon working to the lowest order in Ω_p but to all orders in Ω_s, we can obtain in the steady state

$$c_+ = \frac{\Omega_s[B(O - L) + 2ig^2\omega_m\omega_0]}{B(O^2 - L^2) + 4iLg^2\omega_m\omega_0}, \tag{17}$$

with $O = \kappa - i\delta$, $L = i\Delta_p - ign_0$, and $B = -\delta^2 - i\gamma\delta + \omega_m^2$.

To investigate the optical property of the system, we use the input-output relation $c_{\text{out}}(t) + c_{\text{in}}(t) = \sqrt{2\kappa}c(t)$ [25] to calculate the output field, where $c_{\text{out}}(t)$ and $c_{\text{in}}(t)$ are the output and input operators, respectively. In accordance with the above discussions, we also ignore the quantum properties of $c_{\text{out}}(t)$ and $c_{\text{in}}(t)$. Noticing that the mean value of $c_{\text{in}}(t)$ equals zero, we can obtain

$$\begin{aligned} \langle c_{\text{out}}(t)\rangle &= c_{\text{out}0} + c_{\text{out}+}e^{-i\delta t} + c_{\text{out}-}e^{i\delta t} \\ &= \sqrt{2\kappa}(c_0 + c_+ e^{-i\delta t} + c_- e^{i\delta t}). \end{aligned} \tag{18}$$

From this equation, we see that $c_{\text{out}+} = \sqrt{2\kappa}c_+$. Here $c_{\text{out}+}$ is a parameter in analogy with the linear optical susceptibility [26]. The real part of $c_{\text{out}+}$ exhibits an absorptive behavior, and its imaginary part shows a dispersive property for the reason that the phase of light changes by $\pi/2$ on the reflection.

3. ULF SPECTRUM

In past years, no experimental observations of the Raman active F-mode were reported. Because the F-mode is very close to the Rayleigh line (0 cm^{-1}) and the Rayleigh scattering signal is up to dozens of orders of magnitude higher than the Raman signal, it is impossible to be distinguished from the Rayleigh background scattering in such a low-frequency band. In this section, we provide the discussion of the optomechanical mechanism of the SERS with the pump-probe technology. We demonstrate the Raman signal can be detected at ULF band by using a bad plasmon cavity in a remote Rayleigh line and a pump-probe scheme to amplify the Stokes and anti-Stokes scattering. We focus on the F-mode, though our methods and the results can be generalized to any vibration mode with Raman activity in two-dimensional layered materials and other molecular structures. The enhancement can be realized at room temperature and ultralow laser power, displaying a notable advantage over traditional SERS measurements.

For illustration of the numerical results, we choose realistic experimental parameters. The natural frequencies of the

F-mode of the SGR depend on the length and also the boundary conditions. According to Ref. [20], the resonance frequencies of nanoscale SGR are of the order of gigahertz. Here we choose a suspended nanoscale SGR of dimensions $l = 6$ nm, $w = 0.7$ nm, composed of 162 carbon atoms with the total mass, $m = 3.2 \times 10^{-24}$ kg. The fundamental frequency of a doubly clamped monolayer graphene can be estimated by $\omega_m \approx 3056/l^2$, in which the length is in nanometers, and the frequency is in gigahertz. Thus, we can obtain the frequency $\omega_m \approx 100$ GHz corresponding to 3 cm^{-1}.

The previous work has calculated the absolute Raman response of graphene and graphite via its explicitly frequency-independent Raman matrix element using the method of sample substitution [27]. For the A_g modes, the Raman activity of graphene can reach $R = 10^3 \sim 10^4$ (Å$^4 \cdot$ amu^{-1}). In a realistic plasmon-nanocavity system, the mode volume of the plasmon cavity is estimated to be $V_c \approx 1.5 \times 10^{-6}$ μm^3 [10]. Assuming that the resonance frequency of the plasmon cavity $\omega_c = 330$ THz ($\lambda = 900$ nm), then considering $\omega_m = 100$ GHz, we find that the coupling rate $g = 200 - 600$ GHz.

The lowest energy resonance corresponds to the fundamental F-mode, and the resonator is assumed to be characterized by the mechanical quality factors Q_{SG}, which strongly depend on the temperature. Until now, the highest quality factor observed in monolayer graphene resonators at room temperature was on the order of several hundreds [28–31]. Supposing $Q_{\mathrm{SG}} \approx 200$, we get the mechanical damping rate of SGR as $\gamma = \omega_m/Q_{\mathrm{SG}} = 0.5$ GHz and the lifetime of the F-mode phonon $\Delta t = 1/\gamma = 2$ ns. The plasmonic systems experience strong ohmic losses, namely, they are characterized by very low quality factors, typically $Q_c \approx 10$, placing these systems deep in the bad cavity regime ($\kappa = \omega_c/Q_c = 33$ THz).

The physical origin in such coupled systems can be explained as the four-wave mixing (FWM) process. The simultaneous presence of a pump field and a probe field generates a radiation pressure force at the beat frequency, which drives the motion of the SGR near its resonance frequency. During vibrational motion, the change in polarizability of the SGR leads to a shift of the plasmon resonance frequency at the origin of the parametric optomechanical coupling. The process can be interpreted in a dressed-state picture as depicted in Fig. 2, where the original two levels of cavity $|c\rangle$ split into four dressed states while coupling with the phonon modes ($|M\rangle$ denotes the number states of the SGR mechanical mode). Figure 2(a) represents the phonon-induced three-photon resonance, where the plasmon cavity makes a transition from the lowest dressed level to the highest dressed level by the simultaneous absorption of two photons and the emission of a photon at $\omega_p - \omega_m$. This process can amplify a wave at $\delta = -\omega_m$, which is indicated by the negative absorption of the Stokes peak. Figure 2(b) shows the origin of phonon-induced stimulated Rayleigh resonance, which corresponds to a transition from the lowest dressed level $|c-1, M\rangle$ to the dressed level $|c, M\rangle$. Thus, the gain feature that occurs near $\delta = 0$ can be considered to be a form of stimulated Rayleigh scattering [26]. The rightmost Fig. 2(c) is related to the phonon-induced absorption resonance as modified by the anti-Stokes scattering, which corresponds to $\delta = \omega_m$.

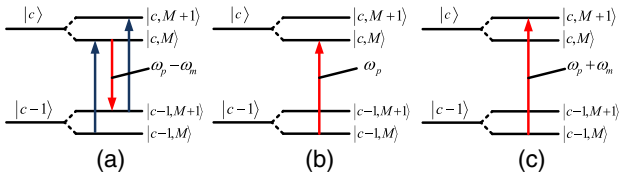

Fig. 2. Energy level diagram of the SGR-plasmon optomechanical system, where M and c denote the number states of mechanical mode and plasmon cavity photon, respectively. The three pictures correspond to the physical processes of (a) Stokes scattering, (b) Rayleigh scattering, and (c) anti-Stokes scattering.

At first, we do not apply the pump field and investigate the phonon-induced stimulated Rayleigh resonance. We depict the absorption spectrum $\mathrm{Re}(c_{\mathrm{out}+})$ of the probe field as a function of the probe-cavity detuning $\delta_c = \omega_c - \omega_s$ for different plasmonic quality factors $Q_c = 2, 5, 10, 20$, with pump field $\Omega_p = 0$ in Fig. 3. The unit of the scattering absorption intensity is an arbitrary unit (a.u.), which is a relative unit of measurement to show the ratio of amount intensity to a predetermined reference measurement. Experimental studies for Raman shift in the SERS usually express the wavenumber of the vibrational mode in cm^{-1}, being related to the angular frequency via $\omega_m/2\pi$ [Hz] $= 10^2 C\delta_c$ [cm^{-1}]; here C is the speed of light. The results show that the plasmon Q factor modulates the shape of the Rayleigh peak. When the plasmonic quality factor decreases, the linewidth increases, and the strength reduces. In the traditional Raman measurements, the incident light hits the sample, while the pump-probe beam hits the plasmon in our scheme. Thus, the Rayleigh peak can be suppressed remarkably due to the strong ohmic losses of plasmon. This indicates that one can remote the Rayleigh line on the spectrum by using an extremely low Q cavity.

Then we study the ULF scattering spectrum with the pump-cavity detuning $\Delta_p = 0$. We set the optomechanical coupling rate at $g = 200$ GHz, corresponding to the Raman activity $R = 10^3$ Å$^4 \cdot$ amu^{-1}. Then we depict the absorption spectrum

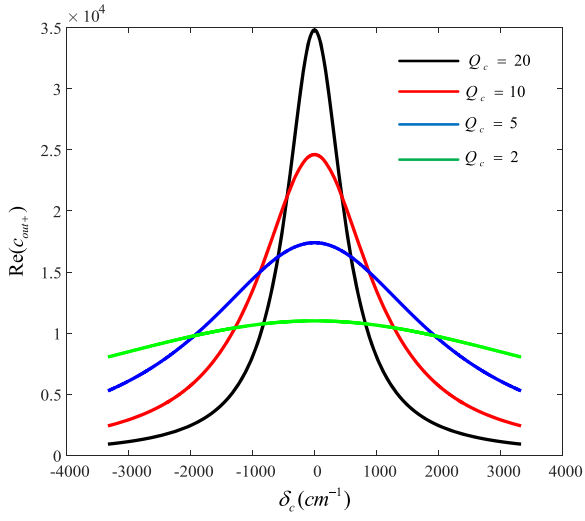

Fig. 3. Strength of Rayleigh scattering on the probing absorption spectrum as a function of the probe-pump detuning δ_c for different quality factors of the plasmon. We set $E_p = 0$; other parameter values are $\Omega_s = 0.1$ THz, $\gamma = 0.5$ GHz.

of the probe pulse as a function of the probe-pump detuning δ for different input pump field intensities, which can be obtained by [10]

$$I = \frac{1}{2}\varepsilon_0 C|E_p|^2. \tag{19}$$

We select $I = 1$ kW/cm^2, 2 kW/cm^2, and 3 kW/cm^2, respectively, in Fig. 4. If the frequency beat of laser δ is close to the resonance frequency of the F-mode, it will start to oscillate coherently and result in Stokes ($\omega_c - \omega_m$) and anti-Stokes ($\omega_c + \omega_m$) scattering of light due to the optomechanical coupling. From Fig. 4, we can clearly see that the scattering spectrum can be modulated effectively by the pump laser. The strength of the Stokes and anti-Stokes peaks increases remarkably by increasing the pump intensity, whereas the shape of the Rayleigh peak remains unchanged. Compared with the previous schemes to detect graphene via SERS, the distinct difference in our scheme is the use of pump-probe technology in the plasmon cavity. The geometries of the scattering peaks are decided by the vibrational damp of the SGR γ and the optomechanical coupling rate g. For the case of a weak pump, the Rayleigh peak is very strong; hence the Stokes and anti-Stokes signals may be submerged in the Rayleigh background. However, as shown by the black curve in Fig. 4, the Raman signal is enhanced remarkably when the pump power rises to $I = 3$ kW/cm^2. In Fig. 4, the Rayleigh peak approaches a horizontal line because its strength is much weaker than the F-mode peak. Here the pump power is about 2–3 orders of magnitude smaller in comparison with traditional SERS techniques [10,23]. This nonlinear effect with weak light provides new opportunities for the nondestructive testing of Raman properties of the bioactive molecules and living organisms.

The pump intensity dependence of the ratio between Raman absorption and Rayleigh strength is depicted in Fig. 5. We obtain the linear relations. The ratio is up to 10 for $I = 10$ kW/cm^2, with the coupling rate $g = 200$ GHz.

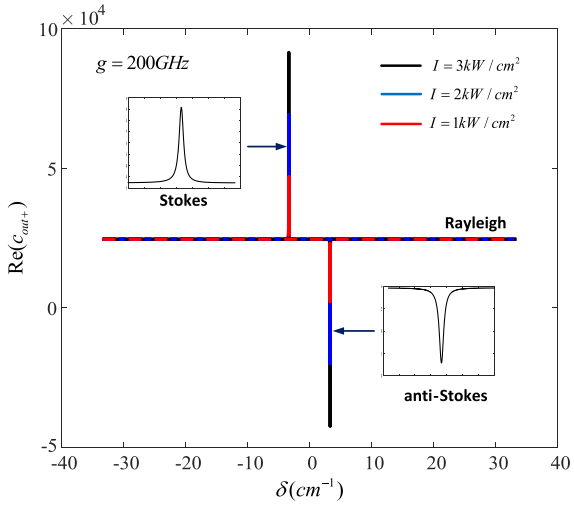

Fig. 4. Plot of absorption spectrum as a function of probe-pump detuning with $R = 10^3$ Å$^4 \cdot$ amu^{-1}, $g = 200$ GHz, $Q_c = 10$, and $\Delta_p = 0$ for $I = 1, 2,$ and 3 kW/cm^2, respectively. Other parameter values are the same as in Fig. 3.

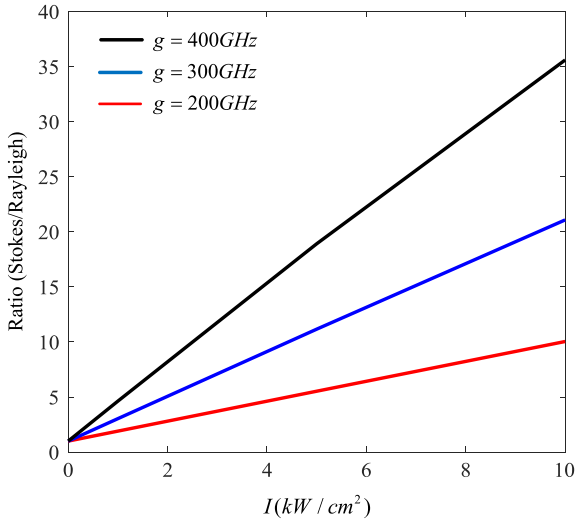

Fig. 5. Pump intensity dependence of the ratio between Raman and Rayleigh scattering strength with different optomechanical coupling rate g.

Hence, we can abstract the Raman signals completely from the Rayleigh background. To study the coupling between the SGR and plasmon, we add the blue line and the black line to show the enhancements for different coupling rates g in Fig. 5. We can find that, in the case of the same pump strength, the Stokes peak becomes stronger by increasing the optomechanical coupling rate. That is to say, we can separate out the signals of the ULF mode from the Rayleigh background more easily under stronger coupling rates g. The plasmon system works in the unresolved -sideband regime ($\kappa \gg \omega_m$). Since the strong coupling mainly comes from the low mechanical frequency ω_m and small volume of the plasmon cavity mode V_c [see Eq. (1)], the enhancement in the unresolved sideband regime can still be achieved by using the optical pump-probe schemes in the surface plasmon cavity.

Basically, because the Stokes and the anti-Stokes Raman signals are much weaker than the Rayleigh peak, the ULF mode detection cannot be achieved by the traditional SERS measurement. However, with the FWM process in plasmon, the ULF mode can be detected on the probing spectrum by combining the two methods. (i) The Rayleigh peak can be suppressed effectively in the low Q plasmon cavity ($Q_c = 10$). (ii) The amplitude of the Raman signal can be enhanced remarkably by increasing the pump laser. One can find the strength of the Raman signal is up to dozens of times higher than the Rayleigh scattering signal.

4. SINGLE NEUTRAL ATOM MASS SENSOR

In this section, we provide the scheme in order to achieve the ultrasensitive mass sensing based on plasmon-assisted pump-probe spectroscopy. Atoms or molecules landing on the surface of the graphene nanoribbon can significantly increase the total mass of the resonator, which will simultaneously reduce the resonance frequency. Applying the concept of effective mass $\omega_m = \sqrt{k/m}$, we can find that the relationship between the frequency shift and the increased mass can be expressed as

$$\Delta m = \frac{2m}{\omega_m}\Delta\omega. \tag{20}$$

Mass sensing is based on monitoring the frequency shift $\Delta\omega$ of ω_m. According to Eqs. (11) and (17), we depict the probe spectrum of the SGR as a function of detuning δ for the pump power $I = 1$ kW/cm^2 by the black curve in Fig. 6. We find that a sharp peak at the position just corresponds to the fundamental frequency of the F-mode. This means that if we first fix the pump field detuning $\Delta_p = 0$ and scan the probe frequency across the exciton frequency ω_c in the spectrum, then we can easily obtain the vibrational frequency of the nanomechanical resonator exactly.

Then we select an Ne atom to deposit onto the surface of the SGR to increase the mass of the graphene nanoribbon. We illustrate this mass sensor scenario in Fig. 1(a). The additional mass modifies the resonance frequency of the system. For the single atom, the resonance frequency shift $\Delta\omega = 0.52$ GHz can be resolved in the spectrum displayed by the blue curve in Fig. 6. We can obtain the total mass of the accreted Ne atom, $\Delta m \approx (2m/\omega_m)\Delta\omega = 3.32 \times 10^{-26}$ kg. The linear relationship between the resonance frequency shift and the numbers of deposited Ne atoms is then given by $\Delta\omega = 0.52n$ GHz (n denotes the atom number). As we select more atoms to deposit onto the SGR sensor, the enhanced peak will exhibit a larger frequency shift on the spectrum. We then plot the 10 atoms induced shift in Fig. 6 by the red curve. The resolution can be obtained by Eq. (20). The minimum detectable frequency shift depends on the full width at half-maximum (FWHM) of the absorption peak, which is approximately 0.5 GHz in Fig. 6. Then considering $\omega_n = 100$ GHz, we can obtain the minimum measurable mass $\Delta m_{\min} = 3 \times 10^{-26}$ kg (30 yg). This sensitivity will provide the possibility of identifying the chemical nature of individual atoms and molecules if single atoms and molecules can be trapped at a specific site on the graphene nanoribbon (for example, using electrochemistry to create trapping sites by locally modifying the carbon lattice [32]).

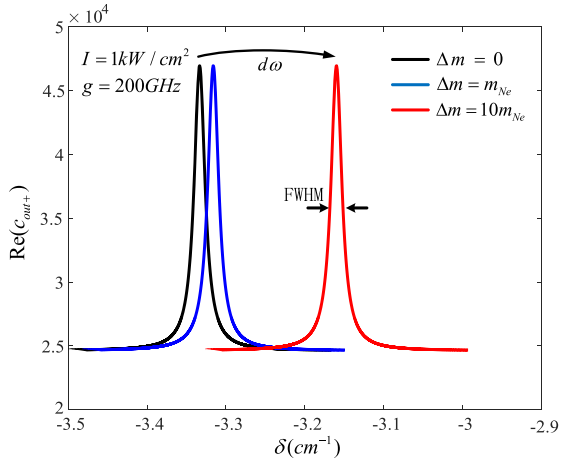

Fig. 6. Absorption spectra of the probe pulse as a function of δ before (black line) and after the binding events of one Ne atom (blue line) and 10 atoms (red line). The frequency shifts induced by additional masses can be well distinguished in the spectra. Here we choose $R = 10^3$ Å$^4 \cdot$ amu^{-1}, $I = 1$ kW/cm^2. Other parameters used are the same as in Fig. 4.

5. SYSTEM NOISES

The main noises in this system include thermomechanical noise and momentum exchange noise.

A. Thermomechanical Noise

In our scheme, the thermal noise of the mechanical motion is the dominant noise source. We now turn to the evaluation of the minimum measurable frequency shift, $\delta\omega$, limited by thermomechanical fluctuations of the SGR. An estimate for $\delta\omega$ can be obtained by integrating the weighted effective spectral density of the frequency fluctuations by the normalized transfer function of the measurement loop. Performing this integration for the case where $Q \gg 1$, we obtain [33]

$$\delta\omega = \sqrt{\frac{\gamma k_B T \Delta f}{E_c}}. \tag{21}$$

Here, $E_c = m\omega_m^2\langle x_c^2\rangle$ represents the maximum drive energy of the SGR, x_c is the maximum root mean square (rms) amplitude producing a predominantly linear response, and Δf is the measurement bandwidth. Experimentally, the measurement time τ is defined by the detection bandwidth $\tau = 1/\Delta f$, which should be selected to be smaller than the lifetime of the SGR oscillator Δt. To obtain the minimum detectable mass, we rewrite Eq. (21) using the expression for δm given in Eq. (20) and supposing $\tau = \Delta t$

$$\delta m \cong \frac{2m}{\omega_m}\delta\omega = \frac{2m\gamma}{\omega_m}\left(\frac{k_B T}{E_c}\right)^{1/2}. \tag{22}$$

In such a measurement, the resonator is driven at a constant mean square amplitude, assuming $x_c = 5$ Å. At room temperature, $T = 300$ K, then considering $\gamma \approx 0.5$ GHz, the constraint for the mass sensor can reach $\delta m = 2.3 \times 10^{-26}$ kg $< \Delta m_{\min}$. The result shows that the thermomechanical noise can be controlled at a level comparable to the claimed sensitivity at room temperature.

On the other hand, the measuring time $\tau = 2$ ns; the mass changing can be detected in such a short time range. Thus, we can use optical pulses to probe the mechanical frequency with ultrahigh time resolution.

B. Momentum Exchange Noise

Indeed, the Q factor of the SGR oscillator is limited by collisions with residual air molecules. We now turn to a discussion of the consequences of momentum exchange in a gaseous environment between the nanomechanical resonator and the gas molecules that impinge upon it. According to kinetic theory, the limit for the mechanical Q factor due to the momentum exchange noise can be expressed as [33]

$$Q_{\max} = \frac{m\omega_m v}{PA}, \tag{23}$$

where P is the air pressure and A is the surface area of the SGR; $v = \sqrt{3k_B T/m_{\text{gas}}}$ and m_{gas} are the rms velocity and mass of gas molecules, respectively. To minimize adsorption of unwanted molecules, we prepare the measurement setup at low pressure, supposing $P = 1$ Torr, then we obtain

Table 1. Parameters of the Plasmon Optomechanical System Used in the Mass Measurement

Parameter	Units	Value
Width of SGR, w	nm	0.7
Length of the SGR, l	nm	6
Fundamental frequency of SGR, ω_m	GHz	100
Frequency of the plasmon, ω_c	THz	330
Raman activity of F-mode, R	$\text{Å}^4 \cdot \text{amu}^{-1}$	10^3–10^4
Volume of plasmon cavity, V_c	μm^3	1.5×10^{-6}
Quality factor for SGR, Q_{SG}	Null	200
Quality factor for plasmon, Q_c	Null	10
Conservative quantum yield, η	Null	0.01
Pump-cavity detuning, Δ_p	Hz	0
Air pressure, P	Torr	1
Temperature, T	K	300

$Q_{\text{max}} = 1.4 \times 10^5 \gg Q_{\text{SG}}$ with $T = 300$ K. Thus, these all-optical mass sensors have the potential to break through the limitation of air pressure restriction and to enhance the sensitivity of mass detection.

Since the thermal noise and the momentum exchange noise can be suppressed effectively at room temperature, the sensitivity is only determined by the FWHM of the optical spectrum. We list all the main plasmon optomechanical parameters in Table 1, and we expect the atomic resolution mass sensor can be achieved under these conditions.

6. CONCLUSION

In the paper, we provide what we believe is the first discussion about the double fields-controlled plasmonic optomechanics for the artificial molecule, namely, an SGR. We investigate the coupling between plasmon and the SGR based on the interaction between the electromagnetic field and the breathing-like F-mode in nanoribbons with Raman activity. Due to the very low Q value of the plasmon cavity, the Rayleigh scattering can be effectively attenuated. Simultaneously, by increasing the pump power, the probe signal can be amplified significantly. Thus the ULF mode signals can be distinctly separated from the Rayleigh background in the absorption spectrum. Based on these results, we propose an experimentally feasible scheme for the mass sensing of a single atom via the mass-induced-shift on the spectrum. This scheme can be realized under ultrashort measurement time and displays notable advantages in contrast to the generic optomechanical systems [34] as follows. (a) The sensitivity strongly depends on the mass of the mechanical resonator. Since the SERS scenarios can be mapped onto the canonical model of cavity optomechanics, we can use the artificial molecular structure with smaller effective mass. Thus, the mass sensitivity can be improved remarkably, from 0.16 fg to 30 yg (about 7 orders of magnitude), compared to the result in Ref. [34]. (b) In the previous works, the high-quality factor is necessary [18]; thus these schemes usually require cryogenic temperatures. But our optical mass sensor can be achieved at room temperature. (c) The plasmonic system works in the bad cavity regime (ultrahigh damping). However, owing to the plasmonic enhancement, there is no requirement for the finesse of the cavity, in contrast to generic optomechanical systems. Finally, we hope that our proposed device can be realized by experiments in the near future.

Funding. National Natural Science Foundation of China (NSFC) (11274230, 11574206); Basic Research Program of the Committee of Science and Technology of Shanghai (14JC1491700).

REFERENCES

1. M. Moskovits, "Surface-enhanced spectroscopy," Rev. Mod. Phys. **57**, 783–826 (1985).
2. A. Otto, I. Mrozek, H. Grabhorn, and W. Akemann, "Surface-enhanced Raman scattering," J. Phys. Condens. Matter **4**, 1143–1212 (1992).
3. M. D. Sonntag, J. M. Klingsporn, L. K. Garibay, J. M. Roberts, J. A. Dieringer, T. Seideman, K. A. Scheidt, L. Jensen, G. C. Schatz, and R. P. Van Duyne, "Single-molecule tip-enhanced Raman spectroscopy," J. Phys. Chem. C **116**, 478–483 (2012).
4. S. M. Nie and S. R. Emory, "Probing single molecules and single nanoparticles by surface-enhanced Raman scattering," Science **275**, 1102–1106 (1997).
5. W. Zhu and K. B. Crozier, "Quantum mechanical limit to plasmonic enhancement as observed by surface-enhanced Raman scattering," Nat. Commun. **5**, 5228 (2014).
6. J. P. Camden, J. A. Dieringer, Y. Wang, D. J. Masiello, L. D. Marks, G. C. Schatz, and R. P. Van Duyne, "Probing the structure of single-molecule surface-enhanced Raman scattering hot spots," J. Am. Chem. Soc. **130**, 12616–12617 (2008).
7. D. Wang, W. Zhu, M. D. Best, J. P. Camden, and K. B. Crozier, "Directional Raman scattering from single molecules in the feed gaps of optical antennas," Nano Lett. **13**, 2194–2198 (2013).
8. R. Zhang, Y. Zhang, Z. C. Dong, S. Jiang, C. Zhang, L. G. Chen, L. Zhang, Y. Liao, J. Aizpurua, Y. Lou, J. L. Yang, and J. G. Hou, "Chemical mapping of a single molecule by plasmon-enhanced Raman scattering," Nature **498**, 82–86 (2013).
9. R. Chikkaraddy, B. Nijs, F. Benz, S. J. Barrow, O. A. Scherman, E. Rosta, A. Demetriadou, P. Fox, O. Hess, and J. J. Baumberg, "Single-molecule strong coupling at room temperature in plasmonic nanocavities," Nature **535**, 127–130 (2016).
10. P. Roelli, C. Galland, N. Piro, and T. J. Kippenberg, "Molecular cavity optomechanics as a theory of plasmon-enhanced Raman scattering," Nat. Nanotechnol. **11**, 164–169 (2016).
11. A. K. Naik, M. S. Hanay, W. K. Hiebert, X. L. Feng, and M. L. Roukes, "Towards single-molecule nanomechanical mass spectrometry," Nat. Nanotechnol. **4**, 445–450 (2009).
12. E. Gil-Santos, D. Ramos, A. Jana, M. Calleja, A. Raman, and J. Tamayo, "Mass sensing based on deterministic and stochastic responses of elastically coupled nanocantilevers," Nano Lett. **9**, 4122–4127 (2009).
13. H. Y. Chiu, P. Hung, H. W. C. Postma, and M. Bockrath, "Atomic-scale mass sensing using carbon nanotube resonators," Nano Lett. **8**, 4342–4346 (2008).
14. K. Jensen, K. Kim, and A. Zettl, "An atomic-resolution nanomechanical mass sensor," Nat. Nanotechnol. **3**, 533–537 (2008).
15. J. Chaste, A. Eichler, J. Moser, G. Ceballos, R. Rurali, and A. Bachtold, "A nanomechanical mass sensor with yoctogram resolution," Nat. Nanotechnol. **7**, 301–304 (2012).
16. M. LaHaye, O. Buu, B. Camarota, and K. Schwab, "Approaching the quantum limit of a nanomechanical resonator," Science **304**, 74–77 (2004).
17. S. Chun, Y. Kim, H. Jin, E. Choi, S. B. Lee, and W. Park, "A graphene force sensor with pressure-amplifying structure," Carbon **78**, 601–608 (2014).
18. J. J. Li and K. D. Zhu, "All-optical mass sensing with coupled mechanical resonator systems," Phys. Rep. **525**, 223–254 (2013).
19. J. J. Li and K. D. Zhu, "Weighing a single atom using a coupled plasmon-carbon nanotube system," Sci. Tech. Adv. Mater. **13**, 025006 (2012).
20. A. Sakhaee-Pour, M. T. Ahmadian, and R. Naghdabadi, "Vibrational analysis of single-layered graphene sheets," Nanotechnology **19**, 085702 (2008).
21. M. Sadeghi and R. Naghdabadi, "Nonlinear vibrational analysis of single-layer graphene sheets," Nanotechnology **21**, 105705 (2010).

22. R. Gillen, M. Mohr, and J. Maultzsch, "Symmetry properties of vibrational modes in graphene nanoribbons," Phys. Rev. B **81**, 205426 (2010).
23. M. K. Schmidt, R. Esteban, A. Gonzalez-Tudela, G. Giedke, and J. Aizpurua, "Quantum mechanical description of Raman scattering from molecules in plasmonic cavities," ACS Nano **10**, 6291–6298 (2016).
24. V. Giovannetti and D. Vitali, "Phase-noise measurement in a cavity with a movable mirror undergoing quantum Brownian motion," Phys. Rev. A **63**, 023812 (2001).
25. D. F. Walls and G. J. Milburn, *Quantum Optics* (Springer-Verlag, 1998), p. 124.
26. R. W. Boyd, *Nonlinear Optics* (Academic, 2008).
27. R. Narula, R. Panknin, and S. Reich, "Absolute Raman matrix elements of graphene and graphite," Phys. Rev. B **82**, 045418 (2010).
28. J. S. Bunch, A. M. van der Zande, S. S. Verbridge, I. W. Frank, D. M. Tanenbaum, J. M. Parpia, H. G. Craighead, and P. L. McEuen, "Electromechanical resonators from graphene sheets," Science **315**, 490–493 (2007).
29. C. Chen, S. Rosenblatt, K. I. Bolotin, W. Kalb, P. Kim, I. Kymissis, H. L. Stormer, T. F. Heinz, and J. Hone, "Performance of monolayer graphene nanomechanical resonators with electrical readout," Nat. Nanotechnol. **4**, 861–867 (2009).
30. A. M. van der Zande, R. A. Barton, J. S. Alden, C. S. Ruiz-Vargas, W. S. Whitney, P. H. Q. Pham, J. Park, J. M. Parpia, H. G. Craighead, and P. L. McEuen, "Large-scale arrays of single-layer graphene resonators," Nano Lett. **10**, 4869–4873 (2010).
31. V. Singh, S. Sengupta, H. S. Solanki, R. Dhall, A. Allain, S. Dhara, P. Pant, and M. M. Deshmukh, "Probing thermal expansion of graphene and modal dispersion at low-temperature using graphene nanoelectromechanical systems resonators," Nanotechnology **21**, 165204 (2010).
32. B. R. Goldsmith, J. G. Coroneus, V. R. Khalap, A. A. Kane, G. A. Weiss, and P. G. Collins, "Conductance-controlled point functionalization of single-walled carbon nanotubes," Science **315**, 77–81 (2007).
33. K. L. Ekinci, Y. T. Yang, and M. L. Roukes, "Ultimate limits to inertial mass sensing based upon nanoelectromechanical systems," J. Appl. Phys. **95**, 2682–2689 (2004).
34. C. Jiang, B. Chen, J. J. Li, and K. D. Zhu, "Mass sensing based on a circuit cavity electromechanical system," J. Appl. Phys. **110**, 083107 (2011).